LM-05K136
August 16, 2005

Zinc Treatment Effects on Corrosion Behavior of 304 Stainless Steel in High Temperature, Hydrogenated Water

S Ziemniak, M Hanson

NOTICE

Zinc Treatment Effects on Corrosion Behavior of 304 Stainless Steel in High Temperature, Hydrogenated Water

S. E. Ziemniak *
M. Hanson

Lockheed Martin Corporation
P.O. Box 1072
Schenectady, New York 12301-1072

* Corresponding author. Tel.: +1-518-395-6887; fax: +1-518-395-7298.
E-mail address: ziemnia@kapl.gov

ABSTRACT

Trace levels of soluble zinc(II) ions (30 ppb) maintained in mildly alkaline, hydrogenated water at 260°C were found to lower the corrosion rate of austenitic stainless steel (UNS S30400) by about a factor of five, relative to a non-zinc baseline test [3] after 10,000 hr. Characterizations of the corrosion oxide layer via grazing incidence X-ray diffraction and X-ray photoelectron spectroscopy in combination with argon ion milling and target factor analysis, revealed that miscibility gaps in two spinel binaries - $Fe(Fe_{1-m}Cr_m)_2O_4$ and $(Fe_{1-n}Zn_n)Fe_2O_4$ - play a significant role in determining the composition and structure of the corrosion layer(s). Although compositions of the inner and outer corrosion oxide layers represent solvus phases in the Fe_3O_4-$FeCr_2O_4$ binary, zinc(II) ion incorporation into both phases leads to further phase separation in the outer (ferrite) layer. Recrystallization of the low zinc content ferrite solvus phase is seen to produce an extremely fine grain size (~20 nm), which is comparable in size to grains in the inner layer and which is known to impart resistance to corrosion. Zinc(II) ion incorporation into the inner layer creates additional corrosion oxide film stabilization by further reducing the unit cell dimension via the substitution reaction:

$$0.2\ Zn^{2+}(aq) + Fe(Fe_{0.35}Cr_{0.65})_2O_4(s) \rightleftharpoons 0.2\ Fe^{2+}(aq) + (Zn_{0.2}Fe_{0.8})(Fe_{0.35}Cr_{0.65})_2O_4(s)$$

The equilibrium constant for the substitution reaction is similar in magnitude to an estimate based on available free energies for $FeCr_2O_4$, $ZnCr_2O_4$, $Fe^{2+}(aq)$ and $Zn^{2+}(aq)$. This interpretation is consistent with the benefits of zinc treatment being concentration dependent.

KEYWORDS: (A) stainless steel, sputtered films; (B) XPS, AES; (C) oxidation

INTRODUCTION

The development of austenitic stainless steels was one of the most significant metallurgical accomplishments of the Twentieth Century. The German word *rostfrei* was, in fact, used by the inventor of this material because the alloy was considered to be … absolutely rustproof in damp air [1]. Subsequent high temperature application to nuclear reactor coolant systems has revealed that austenitic stainless steels corrode at small, but finite, rates. Furthermore, the transport and activation of stainless steel corrosion products has led to the development of Zn(II) ion additions to the coolant of light water reactors as a method to further minimize the consequences of stainless steel corrosion [2].

The outstanding passivity of austenitic stainless steels to a variety of oxidants is associated with the formation of a protective chromite-based oxide, MCr_2O_4. Recently, we characterized the corrosion film formed on 304 stainless steel in hydrogenated water at elevated temperature [3] and found the inner layer to consist of the solid solution $(Ni_{0.2}Fe_{0.8})(Cr_{0.7}Fe_{0.3})_2O_4$. The important point is that this chromite compound is a spinel: its metal cations are located at interstitial sites in the oxygen lattice having two kinds of symmetry – octahedral and tetrahedral. Because the Cr(III) cation has a strong preference for octahedral sites [4], its spinel oxides are observed to be normal spinels in which the divalent metal cations are contained in tetrahedral sites. It follows that the Zn(II) cation, which exhibits a strong tetrahedral site preference [5], will form a $ZnCr_2O_4$ spinel compound that is particularly stable. If no other changes occur, the increased thermodynamic stability of a corrosion oxide, as manifested by a more compact lattice parameter, is expected to provide an increased resistance to diffusion of metal cations and/or oxygen-bearing species, cf. [6], and thereby lower corrosion rate.

It is generally accepted that the corrosion rate of stainless steels in high temperature, deoxygenated water is controlled by diffusion through the inner, chromite-based, corrosion oxide layer, [7] although short circuit paths (such as along grain boundaries or micropores) are involved, rather than the oxide lattice itself. Therefore, to investigate this apparent paradox, an experimental effort was undertaken to quantify the effects of trace levels of zinc(II) additions (30 ppb) to mildly alkaline, hydrogenated water on 304 stainless steel by: (1) lowering the corrosion rate and (2) modifying the corrosion oxide layer.

EXPERIMENTAL

Corrosion specimens of type 304 stainless steel (UNS S30400) were exposed at 260°C in a flowing autoclave facility (10 $cm^3 min^{-1}$) comprised of a one-liter, type 347 stainless steel (UNS S34700) vessel, and fed from stainless steel tanks containing deionized, hydrogen-sparged water. The dissolved hydrogen concentration was 45 cm^3(@STP)/kg water; alkalinity was buffered to maintain pH (@260°C) = 6.70. Similar levels of dissolved hydrogen are maintained in the reactor coolants of nuclear power plants (NPPs): PWRs use ~25 cm^3(@STP)-kg^{-1} and BWRs on hydrogen water chemistry use <25 cm^3(@STP)-kg^{-1}. A packed bed of granular zinc(II) oxide, located upstream of the test autoclave, was used to supply constant, trace levels of soluble zinc(II) ions. Target zinc concentrations (~30 ppb) were achieved by controlling the feedwater temperature, since the solubility behavior of ZnO had been previously determined as a function of temperature [8]. Test shutdowns, along with specimen removals and insertions, occurred intermittently, so that exposure times ranged between 1000 and 10,000 hours.

In anticipation of the precision corrosion film analyses to be performed, one side of each corrosion specimen (5/80 x 3/40 x 1/160) was highly polished (<6 Fin AA) using diamond grit paste. Larger, machined coupons (40 x 3/40 x .0320) were also prepared and exposed along with the polished

specimens. The larger surface area of the former permitted the total quantity of oxidized base metal to be accurately determined via the application of standard chemical descale (*i. e*., gravimetric) methodology.

ANALYTICAL PROCEDURES

After completion of the test exposure period, the larger corrosion coupons were chemically descaled and the smaller corrosion specimens were subjected to three types of analyses to characterize the states of their oxidized surfaces: (a) scanning electron microscopy (SEM) with X-ray spectroscopy (EDX) , (b) grazing incidence X-ray diffraction (XRD) and (c) X-ray photoelectron spectroscopy (XPS). Due to the unique features of the XRD and XPS analyses, these methodologies are discussed below.

Grazing Incidence X-Ray Diffraction (GIXRD)

Approximate thickness and unit cell dimensions of solid phases in the corrosion oxide layer were determined by GIXRD. Because total oxide thicknesses were <1 Fm, the analysis was performed at Brookhaven National Laboratory using Beamline X3B1 of the National Synchrotron Light Source. This station is equipped with parallel beam optics and was operated at an incident X-ray wavelength of 1.14965 D to reduce sample absorption and minimize the fluorescence background. These conditions are ideal for high resolution analysis of thin film samples that cannot be adequately measured by conventional X-ray sources. The wavelength, as well as the detector zero position, was calibrated using a NIST Al_2O_3 standard. The angle of incidence, **N**, was varied between 0.1 and 1.0° in increments of 0.1°. Spectra were collected at 2**2** values between 20 and 68°. Counting time varied between one and two sec, and the step size was always 0.02°.

For X-rays incident on a solid from air, a critical angle ($\mathbf{N}_c$, rad) is known to exist [9], below which total external reflection occurs:

$$\phi_c = (2\delta)^{1/2}$$

where

$$\delta = N_o\left(e^2/2\pi mc^2\right)\left(Z\rho/A\right)\lambda^2 = 2.797x10^6(Z\rho/A)\,\lambda^2$$

and Z is the average atomic number, A is the average atomic mass, **D** is the mass density (g-cm^{-3}) and **8** is the X-ray wavelength (D). Substituting Z, A and **D** values for typical spinel oxides (i.e., $NiCr_2O_4$, $NiFe_2O_4$ and $FeCr_2O_4$) into the above yields an expected critical incidence angle $\mathbf{N}_c$ = 0.25°.

The actual relationship between **N** and penetration depth (D), however, is non-linear and increases rapidly with **N** in the vicinity of $\mathbf{N}_c$, as the source of diffracted X-rays changes from reflection to absorption [9, 10]:

$$D = \left(\frac{\lambda\sqrt{2}}{4\pi}\right)\left[\sqrt{\left(\phi^2 - \phi_c^{\,2}\right)^2 + 4\left(\delta_i\right)^2} + \phi_c^2 - \phi^2\right]^{-1/2}$$

where □i = **8**F/(4**B**) and F is the linear absorption coefficient. The corresponding penetration depth at $\mathbf{N}_c$ is given by

$$D_c = \left(\frac{\lambda}{4\pi\mathrm{F}}\right)^{1/2}$$

Given a **8** value of 1.150 D, application of the Bragg-Pierce law [11] gives F = 442.9 cm^{-1} ($FeCr_2O_4$) and F = 521.1 cm^{-1} ($NiFe_2O_4$), which allows D_c values to be established as 130-145 D. An increase in **N** from 0.2° to 0.3° increases the 'sampling' depth from about 40 to 700 D.

X-Ray Photoelectron Spectroscopy (XPS)

The composition (elemental and oxidation state) of each corrosion specimen was investigated as a function of depth by successively removing surface material by argon bombardment and analyzing the freshly uncovered surface by XPS. This analysis was performed using a Physical Electronics Model 5601 Microfocus ESCA System. Data collection and details of XPS spectral deconvolution (based on the method of target factor analysis, TFA) remain unchanged from that described previously [3]. Due to differences in corrosion oxide morphology between the present test and that encountered previously [3], further details are included here to illustrate the procedure used to convert sputter times into quantified (and verified) sputter depths.

In cases where the corrosion oxide exists as a true film, lacking in microscopic detail, sputter time can be converted into depth by multiplying by an experimentally-derived sputter rate. This result was readily determined by conducting periodic depth profiling experiments on an amorphous silicon dioxide (SiO_2) or tantalum pentoxide (Ta_2O_5) sputter standard having a known thickness. The thickness (1000 D) was independently determined by profilometry. For general purpose work, the relative differences in sputtering rates between SiO_2 (or Ta_2O_5) and the transition metal oxides are estimated assuming that the sputter yield (*i. e.*, atoms per argon ion) is independent of metal oxide. Since sputter rate is related to sputter yield by a specific grouping of physical properties: **D**n/M (**D** is the oxide density, n is the number of atoms per molecule and M is the molecular weight) [12], sputtering rates relative to Ta_2O_5 are readily determined. On this basis, typical corrosion oxide spinels

Fe_3O_4 (0.157 mol-atom-cm^{-3}) and $FeCr_2O_4$ (0.155 mol-atom-cm^{-3}) will sputter at rates within 20% of the rate for Ta_2O_5 (0.130 mol-atom-cm^{-3}).

Stainless steel corrosion films differ from those formed on ideal oxide sputter standards because they possess microscopic features that decrease sputter yield via surface roughening, crystal face orientation and shadowing effects. Therefore, sputter rates were determined by calibration using actual corrosion films whose thicknesses were independently measured. Oxide thicknesses were determined independently by: (1) converting corrosion rates (determined by chemical descaling) into thickness using metal oxide density and (2) microscopically examining a cross-sectioned metallographic mount of the corrosion specimen. The two-step alkaline permanganate/ammonium citrate descaling method, which corrects for base metal attack, as described previously [3], was again used. Corrections for the small losses of oxide scale due to the corrosion release phenomenon were also accounted for by analyzing coupon weight changes prior to descaling. Due to the sub-micron oxide thicknesses expected, sufficient details from an edge-on cross-section were not obtainable at 10,000X magnification. Therefore, the cross-sectioning of a tungsten-coated metallographic mount was performed at an angle of 6° from the surface plane. This technique increased resolution by a factor of 9.6, i.e., $(\sin 6°)^{-1}$.

It is noted that previous applications of the above methodology found that the argon sputtering rate through corrosion films on iron-base CrNi alloys was equal to the Ta_2O_5 sputtering rate divided by a factor between 1.85 and 2.62; the calibration factor increasing with the size of the outer layer crystals [13, 3].

RESULTS

A. SEM

Appearances of the corroded 304 stainless steel specimens corresponding to exposure times between 1000 and 10,000 hours are shown in Fig 1. It is seen that the initial exposure period created a nearly complete surface covering by a base layer of submicron (<0.5 μm), polyhedral crystals. The crystal faces were oriented in such a manner which showed them to be protruding from a smooth substrate. Minor increases in crystal size, along with complete surface coverage and overlapping growth faces, were observed with increasing exposure time.

In situ measurements of oxide crystal composition by EDX proved inconclusive, due to the small crystal size and penetrating nature of the probe. To eliminate substrate interference, crystals from the outer layer were removed using replicating tape prior to performing EDX. Analyses of 10 randomly selected, <0.5 Fm crystals from an 8000 hr specimen (S90) are summarized in Table I. Assuming a single phase spinel to be present indicates that the oxide crystals are predominantly ferrite (<5% chromite) having an average composition $(Ni_{0.1}Zn_{0.5}Fe_{0.4})Fe_2O_4$.

B. Grazing Incidence X-Ray Diffraction

A full scan GIXRD pattern of a 10,000 hr specimen (S70) is shown in Fig. 2 for **N** (grazing incidence angle) = 0.5^o. All peaks correspond to spinel plane reflections. No other crystalline phases, such as unoxidized 304 stainless steel substrate or ZnO, were detected.

The thickness of the spinel oxide corrosion layer was estimated by monitoring the emergence of the 304 stainless steel [111] XRD peak at several incident angles between **N** = 0.3 and 0.7°. The [111] peak (at 2**2** = 32.3°) was selected for analysis because it is the strongest peak and is readily

distinguishable from the nearest spinel [400] peak at 2**2** = 31.85°. As shown in Fig. 3, the [111] peak for 304 stainless steel first appeared at **N** = 0.6°, providing an estimated oxide thickness of 0.22 Fm using the expected relationship between **N** and penetration depth.

Determination of unit cell dimensions of the spinel phase was not straightforward because of two complicating factors: (1) an asymmetric shoulder was present in each spinel peak and (2) corrections to 2**2** were necessary to account for the change in index of refraction between spinel and air when **N** was less than 0.1 radian. The first required that the XRD spectrum be 'preprocessed' by fitting each peak to a sharp and broad component, see Fig. 4. The presence of a broad, asymmetric shoulder on the high angle side of each spinel peak indicates that a second spinel phase, having a smaller crystal size and a more compact unit cell, is present. Since this phenomenon was not observed in our previous GIXRD analysis of 304 stainless steel corrosion films, [3] the asymmetry probably represents a zinc-induced change in the ferrite-based (outer), rather than chromite-based (inner) corrosion layer. Based on fitted half-widths (FWHM, rad.) of the [311] peak, wavelength of X-radiation (**8** = 1.15 D) and **2** = 13°, application of the Scherrer equation

$$\tau = \frac{0.94\lambda}{FWHM \cdot \cos\theta}$$

indicates that mean grain size (τ) for the sharp peaks is 700 D (0.07 Fm), while the broader components correspond to 200 D (0.02 Fm) crystals. Because the indicated size of the larger crystals agrees with the outer oxide ferrite crystals shown in Fig. 1, it is concluded that a direct correspondence exists between the two.

Since the index of refraction of X-rays in the spinel oxide phase was slightly less than unity, all diffraction peaks were shifted to slightly higher angles than those calculated from Bragg's law. In conventional X-ray diffractometry the shift is usually neglected. However, for small incidence angles the Bragg angle shift due to refraction is much higher and must be taken into account when determining accurate lattice spacings. For **N** <0.01 rad, Reference [14] provides the shift in 2**2** as

$$\Delta 2\theta = 2\theta_{obs} - 2\theta_{cor} = \frac{2\delta}{\sin\left(2\theta_{cor}\right)} + \frac{\delta}{\phi}$$

where **)** 2**2** and **N** are in radians. The results of these calculations for **N** = 0.5° are given in Table II. These corrections lowered the measured 2**2** angles by 0.059 to 0.061°. The unit cell dimensions were finally determined from the corrected peak positions by least-squares refinement. The results are provided below in Table II.

To translate the above result into a composition for the zinc-rich (ferrite) spinel, lattice parameter comparisons with the $(Fe_{1-n}Zn_n)Fe_2O_4$ and $(Ni_{1-n}Zn_n)Fe_2O_4$ spinel binaries, based on the measurements of Kanzaki et al. [15] and Leung et al. [16], respectively, are shown in Fig. 5. Recalling that our previous analyses of 304 stainless steel corrosion films had found that the Fe(II)/Ni(II) ion ratio in the outer layer was ~4/1, lattice parameters for these zinc-substituted solid solutions were estimated by linear interpolation (see dashed line in Fig. 5). In this manner, the calculated lattice parameter (8.396 D) is seen to intersect the estimated curve around $n \sim 0.2$, a value low in comparison to that found by EDX ($n \sim 0.5$).

It is possible to improve upon the n = 0.2 zinc estimate by allowing for small amounts of Cr(III) in the outer layer. Based on its effect in the $Fe(Fe_{1-m}Cr_m)_2O_4$ [17] and $Ni(Fe_{1-m}Cr_m)_2O_4$ [18] spinel binaries, lattice parameter is expected to decrease by about 0.007 Å for an increase in m from zero to 0.05. At this level, the estimated Zn(II) content of the larger ferrite-based crystals increases to >0.3.

On the other hand, the [311] spinel peak for the second ferrite phase shown in Fig. 4 occurs at a 2**2** value higher by ~0. 1°, resulting in a lattice parameter a_0 ~ 8.366 Å. Although this estimate is insufficient to provide an accurate estimate of composition, the lower lattice parameter of the smaller crystals is consistent with a ferrite phase having a lower Zn(II) content and higher Cr(III) content than the larger crystals in the outer layer.

To summarize, the GIXRD analyses provide evidence that the outer layer is split into *two* ferrite-based components; the larger crystals (>0.1 μm) having a higher zinc content, i.e., $(Fe, Ni)_{1-n}Zn_nFe_2O_4$, n>0.3, than the smaller crystals (0.02 μm) having a lower zinc content, i.e., n<0.1. Such behavior suggests that Zn(II) ion incorporation into the ferrite-based outer layer induces immiscibility and causes the low-zinc solvus phase to nucleate as extremely fine crystals (~0.02 μm), whose size approaches that of the (known protective) chromite-based crystals in the inner layer.

C. Argon Ion Sputter Gun Calibration for Depth Profiling XPS Analyses

Two additional, independent estimates of corrosion oxide thickness were obtained by: (1) applying chemical descale analyses to quantitatively remove the corrosion oxide from corrosion coupons and (2) examining a cross-sectioned metallographic mount of a corrosion specimen. Table III summarizes the amounts of corrosion measured on the larger size coupons (0.4078 dm^2 per coupon) exposed

simultaneously with the smaller, polished specimens. A least-squares fit of the corrosion data to a parabolic rate expression yields $K_p = 0.233 \pm 0.031$ mg dm^{-2} $hr^{-1/2}$.

A small correction was applied to account for the difference between the amount of metal oxidized (i.e., corroded) and the oxidized metal inventory in the adherent metal oxide corrosion layer (i.e., scale). This correction was determined by comparing the increase in specimen weight (w) caused by testing with that expected for two limiting cases: complete retention and complete release of the corrosion scale. In the case of zero release

$$w_f = w_i + w_O + w_{Zn}$$

where w_f and w_i refer to the final (post-test) and initial (pre-test) weights, respectively, and w_O and w_{Zn} refer to the respective weights of oxygen and zinc picked up by the corrosion coupons. Since the metal oxides formed during the corrosion process are known to be spinels, AB_2O_4, whose overall composition is known from Table V to be $(Ni_{0.11}Zn_{0.24}Fe_{0.65})(Cr_{0.43}Fe_{0.57})_2O_4$, the expected oxygen and zinc contents are 27.7 wgt % and 6.8 wgt %, respectively. Thus, the zero release case may be rewritten as:

$$w_f - w_i = 0.527\ (w_{dl})$$

where w_{dl} refers to the descaled weight loss, i.e., metals oxidized. In the case of complete release

$$w_f - w_i = -(w_{dl})$$

By expressing the post-test – pre-test weight difference as a fraction of the maximum change between the zero and complete release limiting cases, i.e., 1.527 x w_{dl}, the fraction of corroded alloy released to the water was determined. The results of these calculations are summarized in the final columns of Table III. These calculations indicate that approximately 20% of the corroded metal was released to the water. Upon subtracting the indicated amounts of release from the metals oxidized and converting

to metal oxide, the surface density of corrosion oxide on the 10,000 hr coupon becomes 21.9 mg dm^{-2}. Assuming an oxide density of 5.2 g cm^{-3} provides an estimated oxide thickness, t = 0.42 Fm.

A second estimate of oxide thickness was obtained by examining a tungsten-coated, cross-sectioned metallographic mount of a 10,000 hr corrosion specimen (S66). The tungsten coating served to define the outer oxide/water interface and to ensure its integrity during the sectioning process. As mentioned previously, a low angle cut relative to the surface plane (6°) provided an increase in resolution by nearly a factor of 10. The resulting color-coded elemental Auger intensity maps for Fe, Cr, Ni, O, Zn and W for one segment of the cross-sectioned corrosion film are shown in Fig. 6. On this basis it is found that t = 0.27 Fm.

Averaging the GIXRD (0.22 Fm), gravimetric (0.42 Fm) and cross-sectioning (0.27 Fm) results for the 10,000 hr specimens results in an estimated oxide thickness of 0.30 Fm for the 10,000 hr test specimens. A calibration factor for the argon ion sputter gun was, therefore, defined to provide the XPS O(1s) depth on the 10,000 hr specimen as 0.30 Fm. For the Table IV data, this factor was equivalent to the Ta_2O_5 thickness divided by 1.11. This factor, which is smaller than found previously [3, 13], is consistent with the presence of smaller-size oxide crystals (#0.5 Fm).

Besides providing information on oxide thickness, the elemental intensity maps of the cross-sectioned metallographic mount revealed a number of compositional details: (1) both Cr and O maps clearly identified the alloy/inner oxide and inner oxide/outer oxide interfaces, (2) the Fe, O and W maps revealed the porous nature of the iron oxide-rich outer layer, and (3) the grainy texture, i.e., variability, of Zn throughout the inner and outer layers is also revealed, although lower concentrations of Zn, Fe and O in the outer layer may be a consequence of signal dilution by W. The Ni map deserves special

mention since nickel composition throughout the outer and inner layer oxides is low and rather uniform except in the zone closest to the interface between the inner oxide and alloy substrate. Here nickel concentrations are greater than in the base alloy. This region also coincides with lower oxygen concentrations. The apparent presence of metallic nickel may be a consequence of zinc incorporation/substitution: the Ni(II) cations in the inner layer chromite that are replaced by Zn(II) cations are unstable, undergo reduction and recrystallize as Ni(0).

D. X-Ray Photoelectron Spectroscopy with Argon Ion Milling

Typical elemental composition versus depth profiles are shown in Figs. 7a and b for specimens having exposure times of 5000 and 10,000 hr, respectively. As expected, the major elements detected were oxygen, iron, chromium, zinc and nickel. Significant levels of carbon were also found on the surfaces of all specimens. Because the initial ion milling operation reduced the carbon signals to trace levels, it was concluded that carbon was present as an adsorbed layer of hydrocarbon contamination, and was neglected when performing further analyses.

The presence of an outer layer corrosion oxide, i.e., the observed polyhedral crystals, growing on the specimen surfaces in Fig. 1, tended to manifest themselves by causing elongated 'tails' in the oxygen profiles, see Fig. 7. Therefore, estimates of oxide thickness were obtained from the inflection point in each oxygen, i.e. O(1s), profile: a maximum in the first derivative represents the depth at which ion milling of the oxide layer exposed metal substrate at the most rapid rate. These results are summarized in Table IV. For consistency with the expected corrosion kinetics, increases in oxide thickness were correlated with a parabolic growth rate expression:

$$D_{O1s} = K_{po}(t)$$

By least-squares analysis, it was found that K_{po} = 40 " 16 D hr^{-} , so that an oxide thickness of 0.40 " 0.16 Fm is predicted after an exposure period of 10,000 hr. Applying an oxide density ~5.2 g cm^{-3} recasts the parabolic growth as an oxide surface density: K_{ps} = 0.210 ± 0.083 mg (spinel) dm^{-2} hr$^{-1/2}$.

The above oxide thickness estimates were refined and speciated by TFA; speciated profiles for the 5000 and 10,000 hr specimens being shown in Figs. 8 and 9, respectively. To facilitate *oxide* comparisons, two plots were generated for each speciated composition profile: (a) a cross-hatched/solid split between oxidized metal and unoxidized metal, and (b) the indicated stoichiometry of the spinel oxide $(Ni_yZn_zFe_{1-y-z})(Fe_{2-x}Cr_x)O_4$. This information is summarized in a tabular manner and integrated numerically to quantify the overall amount and stoichiometry of the corrosion film, see Tables V and VI.

The above results indicate that 304 stainless steel may have corroded selectively, with iron and nickel being protected at the expense of chromium. Composition of the corrosion oxide versus alloy substrate, by constituent, is: 62 vs. 72 (wgt % iron), 7 vs. 9 (wgt % nickel) and 31 vs. 19 (wgt % chromium). However, as will be discussed, a more likely interpretation is that corrosion occurred non-selectively, chromium was retained in the oxide (due to its lower solubility in aqueous solution [19]) and a portion of the oxidized iron was selectively released to the water. Oxidized nickel was both released and recrystallized to nickel metal.

DISCUSSION

A. Kinetics of 304 Stainless Steel Corrosion

Based on a correlation of the chemical descale results presented in Table III, zinc treatment is observed to significantly reduce the corrosion rate of 304 stainless steel; a comparison of the parabolic rate

constants for non-selective oxidation yielding K_p = 0.233 ± 0.031 mg alloy dm^{-2} $hr^{-1/2}$ (zinc test) vs. 1.16 ± 0.05 (baseline test [3]), see Fig. 10. Thus, the addition of 30 ppb soluble zinc(II) ions to mildly alkaline, hydrogenated water at 260°C lowered the corrosion rate by about 75%.

The effectiveness of zinc in lowering the corrosion rate is expected to be concentration dependent; higher concentrations producing greater reductions. Fig. 11 shows that our results are consistent with the reductions obtained by Haginuma et al. [20], who tested 304 stainless steel in hydrogenated pure water at 288°C and used Zn(II) ion levels of 0, 0.2 and 0.8 Fmolal. (1 Fmolal = 65 ppb Zn.)

B. Characteristics of Corrosion Layer

The corrosion of 304 stainless steel in hydrogenated water at elevated temperature was previously shown to result in the formation of a two-layered, corrosion oxide film [3]. The oxide is classified as a spinel: AB_2O_4, where A represents a divalent cation and B represents a trivalent cation. No other oxide phases were detected. In the outer layer, Fe(III) is the main B constituent, while both Cr(III) and Fe(III) are present in the inner layer. The existence of two spinel oxide layers is believed to be a manifestation of immiscibility in the Fe_3O_4-$FeCr_2O_4$ binary [3].

Zinc treatment leads to incorporation of Zn(II) cations into the growing ferrite-rich, as well as the chromite-rich, solvus phases, and a corresponding reduction in thickness of the corrosion layer; for example, 0.30 Fm vs. 1.3 Fm after 10,000 hr in the respective zinc and non-zinc tests. Zinc-induced modifications to the ferrite-rich phase, however, are the most noticeable and are explained on the basis of immiscibility in the Fe_3O_4 (magnetite) - $ZnFe_2O_4$ (franklinite) spinel binary. Compositional details of each corrosion layer are discussed below.

Ferrite-Rich Solvus

The outer layer ferrite crystals were much smaller in size compared to previous results from the baseline test [3], i.e., <0.5 Fm vs. ~10 Fm. Compositions of these crystals obtained by EDX analyses suggests that Zn(II) replaced Fe(II) in the A-cation sites; the measured distribution being 50 mol% Zn, 40 mol% Fe and 10 mol% Ni. XPS analyses confirmed this result: 70 mol% Zn, 20 mol% Fe and 10 mol% Ni. The B-cation sites remained populated mainly by Fe(III), as EDX analyses of isolated, <0.5 Fm crystals found <5 mol% Cr(III). Thus, zinc treatment did not significantly alter the trivalent cation composition of the outer layer. An increase in the unit cell dimension from 8.387 D in the baseline test [3] to 8.396 D (see Table II) is consistent with zinc(II) ion incorporation into the ferrite, vis-à-vis the chromite.

High Zn(II) ion levels in the ferrite-based outer layer are somewhat unexpected, since magnetite is a predominately inverse spinel [21] and zinc ferrite (franklinite) is a normal spinel [22]. Therefore, difficulty in mixing is expected. This difficulty is manifested by a miscibility gap in the $(Fe_{1-n}Zn_n)Fe_2O_4$ binary, in which a high zinc content ferrite establishes equilibrium with a low zinc content ferrite. By examining naturally-occurring mineral deposits of franklinite, which contained ex-solution lamellae of magnetite within the franklinite matrix, Graydon and Kirk [23] concluded that the ex-solution texture is consistent with the existence of a miscibility gap and tentatively fixed the critical solution point at 800°C, $n_1 = n_2 = 0.2$. Application of a thermodynamics-based mixing model for spinels [24] predicts a solvus composition $n_1 = 0.05$ and $n_2 = 0.6$ at 300°C.

Characteristics of a low Zn(II) content ferrite-based spinel in the outer layer were inferred from GIXRD and speciated XPS vs. depth profiles. The latter profiles showed that the zinc stoichiometry in the outer layer "bottomed out" near the composition $n \sim 0.05$ before increasing to its $n = 0.2$ value in

the inner layer. When this result is integrated with information on crystal size obtained by GIXRD, the beneficial nature of zinc treatment is explained: the base portion of the outer layer (closest to the inner layer) is composed of extremely fine-grained crystals (~0.02 Fm) whose close packing enhances the barrier for ingress of water already provided by the closely-packed chromite grains having only slightly smaller sizes (*i. e.*, ~0.01Fm).

Chromite-Rich Solvus

On the other hand, the size range of crystals in the non-porous, tightly-adherent inner layer remained about the same as in the baseline test (~0.01µm). Iron ion replacement by zinc was also observed in A-cation sites of the inner layer spinel: the distribution being 20 mol % Zn, 70 mol % Fe and 10 mol % Ni. The Cr(III)-Fe(III) split in the B-cation sites, however, was approximately 65-35, nearly the same as in the baseline test.

Mainly because of decreased amounts of outer layer film relative to inner layer film, the integrated composition of the entire corrosion film was found to be 57.1 wgt % Fe, 28.3 wgt % Cr, 8.4 wgt % Zn and 6.1 wgt % Ni. When zinc is excluded and the results are renormalized, the oxide is seen to be depleted in iron (62.4 wgt % in corrosion film *vs*. 72.4 wgt % in base metal), enriched in chromium (30.9 wgt % in corrosion film *vs*. 19.0 wgt % in base alloy) and depleted in nickel (6.7 wgt % in corrosion film *vs*. 8.6 wgt % in base alloy). A material balance for chromium, however, reveals that the amounts of Cr(III) found in the corrosion layer (via Table V) can be accounted for by assuming non-selective oxidation of the corrosion measurements in Table III and complete retention of oxidized chromium in the corrosion layer (*i.e.*, to within 0.2 mg Cr(III) dm^{-2}). Therefore, the above behavior is consistent with a non-selective corrosion mechanism during which iron and nickel are selectively released to the water by the corrosion release phenomenon. Oxidized nickel was also depleted by

recrystallization to the metallic state. In a similar manner, a material balance for iron in the Table V results indicates that 45% of the oxidized iron had been released to the water. Since iron represents 72% of the corroded metals, the XPS results are consistent with a corrosion release of ~30%. This result is consistent with the result obtained by gravimetric analyses in Table III, *i.e.*, ~20%.

Auger microprobing of a cross-section of the corrosion film found elevated nickel levels at the alloy substrate/inner layer interface. This behavior indicates that Ni(II) ion replacement by Zn(II) also occurred and provided a path for recrystallization of Ni(II) back to elemental nickel.

C. Zn(II) Equilibrium with Inner Layer

The relatively constant Zn(II) content of the corrosion oxide layer found by the integrated, speciated XPS profiles (8.4 wgt. %, see Table V), in response to maintenance of a constant concentration of Zn(II) ions in the aqueous phase (30 ppb), indicates that zinc accommodation may be limited by a thermodynamic equilibrium. Note that the absence of a zinc(II) ion concentration gradient across the inner oxide layer (see Figs. 8 and 9) lends support to the assumption that Zn(II) ion uptake is at equilibrium. This condition will occur if the kinetics for the substitution reaction are more rapid than for the corrosion reaction. If, as a first order approximation, the Fe(III) and Ni(II) ion content of the chromite-rich solvus is neglected, Zn(II) ion incorporation into the inner layer spinel may be described by the equilibrium for

$$0.2\ Zn^{2+}(aq) + FeCr_2O_4(s) \text{ W } 0.2\ Fe^{2+}(aq) + (Zn_{0.2}Fe_{0.8})Cr_2O_4(s)$$

The equilibrium constant (K_{eq}) is given by

$$K_{eq} = \frac{\left[Fe^{2+}(aq)\right]^{0.2}}{\left[Zn^{2+}(aq)\right]^{0.2}}$$

Soluble levels of zinc and iron in the present test were determined by ICP-MS to be 30 and 1.5 ppb, respectively. Based on the known hydrolytic behavior of these ions [7], pH(T) and temperature, it is estimated that $[Zn^{2+}(aq)]/[Zn_{tot}] = 0.00033$ and $[Fe^{2+}(aq)]/[Fe_{tot}] = 0.026$. Substituting into the above gives K_{eq} (533 K) = 1.32 for the hypothesized zinc substitution reaction.

An independent estimate of K_{eq} for the substitution reaction may be obtained from the free energies of $FeCr_2O_4$ and $ZnCr_2O_4$, assuming that the end-member chromites mix ideally. The latter assumption is believed to be valid [24], since both spinels possess a normal lattice configuration. Therefore, the change in free energy for

$$(1\text{-}z)\ FeCr_2O_4(s) + z\ ZnCr_2O_4(s) \rightleftharpoons (Zn_zFe_{1-z})Cr_2O_4(s)$$

may be approximated by

$$\Delta G^{\circ}_{mix} = RT\left[z\ \ln\ z + (1-z)\ln(1-z)\right] = -2.22\ kJ\ mol^{-1}$$

when z = 0.2 at T = 533.15 K. These results allow ΔG° for the zinc substitution reaction to be rewritten

$$\Delta G^{\circ}(533\ K) = 0.2\left[\Delta G^{\circ}_f\left(Fe^{2+}(aq)\right) - \Delta G^{\circ}_f\left(Zn^{2+}(aq)\right)\right] + 0.2\left[\Delta G^{\circ}_f\left(ZnCr_2O_4\right) - \Delta G^{\circ}_f\left(FeCr_2O_4\right)\right] - 2.22\ kJ\ mol^{-1}$$

The calculations are completed by applying compiled thermodynamic properties (see Table VII). It is noteworthy that this revised set is internally consistent for the family of transition metal chromites and is based on standard molar entropies obtained from recent low temperature heat capacity measurements where all magnetic transitions have been taken into account, cf. [25, 26]. In this manner, ΔG° (533 K) = -8.70 kJ mol^{-1}. Invoking the relationship between ΔG° and K_{eq} (*i.e.*, $\Delta G^{\circ} = -RT \ln K_{eq}$) results in a

predicted K_{eq} = 7.13, which is of the same magnitude as that obtained experimentally. Given the approximations associated with both K_{eq} values, it is concluded that closure has been demonstrated relative to the existence of a zinc substitution reaction equilibrium.

SUMMARY/CONCLUSIONS

The corrosion rate of 304 stainless steel in mildly alkaline, hydrogenated water is lowered by the maintenance of trace levels of soluble zinc(II) ions (~30 ppb) by about a factor of five relative to that in a non-zinc baseline test. The effectiveness of zinc treatment appears to be caused by incorporation of Zn(II) ions into the ferrite-based solvus phase that recrystallizes from solution to form the outer corrosion layer. Replacement of Fe(II) by Zn(II) increases the oxide nucleation rate, and results in the formation of a larger number of smaller sized, ferrite-based crystals at the base of the outer layer closest to the inner layer. Since the grain size of these crystals is comparable to that in the inner layer, an enhanced barrier is created to retard ingress of water/oxidants.

The above conclusions are supported by corrosion/release rates determined by application of chemical descaling-gravimetric analyses and composition/structural details of the corrosion oxide layer(s) determined by application of scanning electron microscopy, grazing incidence X-ray diffraction and X-ray photoelectron spectroscopy/ion milling. The value of the latter analytical tool was enhanced considerably by including target factor analyses (TFA), an advanced methodology that allowed metal ion oxidation state profiles to be obtained and additional conclusions to be made regarding selectivity of the corrosion and release processes:

1. Corrosion of 304 stainless steel occurs non-selectively and follows parabolic kinetics, the parabolic rate constant being 0.233 mg (alloy) dm^{-2} $hr^{-1/2}$ at 260°C.

2. Substitution of Fe(II) by Zn(II) ions occurs in the outer (ferrite-based) and inner (chromite-based) corrosion oxide layers, which represent solvus phases in the $Fe(Fe_{1-n}Cr_n)_2O_4$ binary.

3. Outer layer formation, which occurs by a solution/recrystallization mechanism, is altered by the presence of soluble Zn(II) ions: (a) the nucleation rate of ferrite-based oxide crystals is increased, resulting in formation of a sub-layer composed of a larger number density of extremely fine crystals (~20 nm) having the composition $(Fe, Ni)_{1-n}Zn_nFe_2O_4$, $n = 0.05$, (b) due to a miscibility gap in the $(Fe_{1-n}Zn_n)Fe_2O_4$ binary, additional crystallization creates a zinc-rich ferrite ($n = 0.6$) whose crystals are much larger (0.1 – 0.5 μm), but much smaller than observed in the absence of zinc, and (c) a sub-layer structure is created in which the low-zinc phase is located adjacent to the inner layer and the high-zinc phase is adjacent to the water-oxide interface.

4. Uptake of Zn(II) ions by the inner layer also occurs by substitution of Fe(II) by Zn(II) ions. An estimate of the equilibrium constant for the substitution reaction is shown to be consistent with one calculated by applying compiled thermodynamic properties. The Zn(II) ion stoichiometry of the inner oxide depends on the ratio of soluble Zn(II) and Fe(II) ions in the aqueous phase.

ACKNOWLEDGEMENT

The professional assistance of the following individuals is gratefully acknowledged: Dr. Y. Gao (grazing incidence XRD, General Electric Co. Global Research Center), Dr. H. M. Tunison (chemical descale analysis), G. M. Neugebauer (SEM) and A. E. Ferguson (met mount).

REFERENCES

[1] B. Strauss, Proc. ASTM 24 (1924) 208

[2] L.W. Niedrach and W.H. Stoddard, Corrosion 42 (1986) 546

[3] S. E. Ziemniak and M. Hanson, Corros. Sci. 44 (2002) 2209

[4] J. D. Dunitz and L. E. Orgel, J. Phys. Chem. Solids 3 (1957) 318

[5] A. Navrotsky and O. J. Kleppa, J. inorg. nucl. Chem. 29 (1969) 2701

[6] A. G. Crouch and J. Robertson, Acta metall. mater. 38 (1990) 2567

[7] J. Robertson, Corros. Sci. 32 (1991) 443

[8] S. E. Ziemniak, PowerPlant Chem. 3 (2001) 193

[9] G. H. Vineyard, Phys. Rev. B26 (1982) 4146

[10] M. F. Toney, T. C. Huang, S. Brennan and Z. Rek, J. Mater. Res. 3 (1988) 351

[11] R. Jenkins and R. L. Snyder, Introduction to X-Ray Powder Diffractometry, John Wiley & Sons, New York, 1996

[12] M. P. Seah and C. P. Hunt, J. Appl. Phys. 56 (1984) 2106

[13] R. K. Wild, Surf. Interface Anal. 14 (1989) 239

[14] G. Lim, W. Parrish, C. Ortiz, M. Bellotto and M. Hart, J. Mater. Res. 2 (1987) 471

[15] T. Kanzaki, K. Kitayama and K. Shimokoshi, J. Am. Ceram. Soc. 76 (1993) 1491

[16] L. K. Leung, B. J. Evans and A. H. Morrish, Phys. Rev. B 8 (1973) 27

[17] S. E. Ziemniak and R. A. Castelli, J. Phys. Chem. Solids 64 (2003) 2081

[18] S. E. Ziemniak, A. R. Gaddipati and P. C. Sander, J. Phys. Chem. Solids 66 (2005) 1112

[19] S. E. Ziemniak, M. E. Jones and K. E. S. Combs, J. Solution Chem. 27 (1998) 33

[20] M. Haginuma, S. Ono, K. Takamori, K. Takeda, K. Tachibana and K. Ishigure, Zairyo to Kankyo 46 (1997) 565

[21] J. Nell, B. J. Wood and T. O. Mason, Amer. Mineral. 74 (1989) 339

[22] H. St. C. O'Neill, Eur. J. Mineral. 4 (1992) 571

[23] J. W. Graydon and D. W. Kirk, Met. Trans. 19B (1988) 919

[24] H. St. C. O'Neill and A. Navrotsky, Amer. Mineral. 69 (1984) 733

[25] S. Klemme, H. St. C. O'Neill, W. Schnelle and E. Gmelin, Amer. Mineral. 85 (2000) 1686

[26] D. J. Wesolowski, S. E. Ziemniak, L. M. Anovitz, M. L. Machesky, P. Benezeth and D. A. Palmer, Chapter 14 in Aqueous Systems at Elevated Temperatures and Pressures; Physical Chemistry in Water, Steam and Hydrothermal Solutions, D. A. Palmer, R. Fernandez-Prini and A. H. Harvey, eds. Elsevier (2004)

Table I

Composition of Oxide Crystals in Surface Layer
Stripped from 8000 hr Exposure Corrosion Specimen (S90)

Crystal No.	Metal Ion Content, Atom%			
	Fe	Cr	Ni	Zn
1	74.5	-	7.0	18.5
2	70.4	6.5	3.5	19.6
3	75.6	0.3	6.6	17.5
4	76.5	0.4	1.7	21.4
5	78.6	0.3	3.2	17.9
6	79.2	-	6.4	14.4
7	74.0	-	0.7	25.3
8	80.5	0.6	6.6	12.3
9	75.1	0.2	3.8	20.9
10	76.9	2.3	3.2	17.6
Avg.	76.1"2.8	1.1"1.9	4.3"2.1	18.5"3.4

Table II

Spinel Oxide Diffraction Peaks
Observed on 304 Stainless Steel Specimen (S70)
by Grazing Incidence X-Ray Diffraction (**N** = 0.5°)

Reflection Plane Indices, hkl	$2\theta_{obs}$	$2\theta_{cor}$
220	22.379	22.318
311	26.306	26.246
222	27.498	27.438
400	31.857	31.797
422	39.281	39.221
511	41.771	41.711
440	45.674	45.615
620	51.433	51.374
533	53.474	53.415
622	54.143	54.084
642	61.784	61.725
553	63.605	63.546
800	66.579	66.520
	Unit Cell Lattice Parameter, D	8.3956(6)

Table III

304 Stainless Steel Corrosion and Release Estimates
Obtained by Gravimetric Analyses

Exposure Time, hrs	Total Corrosion* mg (metal) dm^{-2}	Weight Change During Test, mg dm^{-2}	Zero Release Wgt. Change, mg dm^{-2}	Corrosion Release, %
1000	7.31 ± 2.44	5.31	3.85	**
2000	11.65 ± 0.91	4.72	6.14	8
5000	12.77 ± 0.93	4.28	6.73	13
5000	18.21 ± 1.95	-0.28	9.60	36
8000	23.64 ± 1.98	0.92	12.46	32
10,000	20.35 ± 1.76	5.89	10.72	16

* Average of triplicate coupons.
** Pickup of unknown material indicated.

Table IV

Surface Oxide Layer Thickness of Type 304 Stainless Steel
Based on Intensity of O(1s) XPS Peak

Exposure Time, hrs.	O(1s) Depth, Å
1000	2130
2000	2455
5000	3935
5000	1555
8000	2815
10,000	4080

Table V

304 Stainless Steel Corrosion Film Characterization
by Integration of Speciated Composition Profile

Exposure Time, hr	Metal Ion Content mg dm^{-2}	Distribution, wgt% Fe(II,III)	Cr(III)	Ni(II)	Zn(II)
1000 (S86)	6.67	63.2	24.7	5.2	6.9
2000 (S82)	10.40	61.8	26.6	4.7	7.0
5000 (S74)	7.99	61.6	25.6	4.7	8.1
5000 (S96)	8.50	54.5	31.2	2.0	12.2
8000 (SX98)	9.82	47.8	31.6	11.0	9.6
10,000 (SX76)	15.82	53.9	30.1	9.1	6.8
	avg:	57.1 ± 5.5	28.3 ± 2.8	6.1 ± 2.8	8.4 ± 1.9
	avg (w/o Zn)	62.4	30.9	6.7	--
	304 SS assay, normalized	72.4	19.0	8.6	--

Table VI

Spinel Composition $(Ni_yZn_zFe_{1-y-z})(Fe_{2-x}Cr_x)O_4$ of
Surface and Inner Corrosion Layers on 304 Stainless Steel

Exposure Time, hrs.	Outer Layer						Inner Layer		
	Surface			Sub-Surface					
	y	z	x	y	z	x	y	z	x
1000 (SX92)	0.30	0.50	0.20	0.30	0.05	0.05	0.30	0.20	1.35
2000 (SX86)	0.30	0.60	0.20	0.30	0.05	0.05	0.30	0.25	1.35
5000 (SX82)	0.30	0.60	0.30	0.30	0.05	0.05	0.30	0.20	1.55
5000 (SX104)	0.05	0.60	0.40	0.25	0.20	0.25	0.30	0.25	1.60
8000 (SX98)	0.20	0.70	0.40	0.25	0.20	0.25	0.30	0.30	1.40
10,000 (SX76)	0.30	0.60	0.20	0.25	0.10	0.05	0.30	0.30	1.30
avg	0.25	0.60	0.30	0.25	0.10	0.10	0.30	0.25	1.40

Table VII

Thermochemical Properties for Select
Chromium(III)-Based Oxides at 298.15 K [26]

Species	$C_p^\circ(298)$	$S^\circ(298)$	$\Delta H_f^\circ(298)$	$\Delta G_f^\circ(298)$
Cr_2O_3	126.47	82.84	-1130.11	-1048.97
$FeCr_2O_4$	136.39	152.20	-1436.88	-1337.50
$ZnCr_2O_4$	129.00	126.60	-1540.74	-1429.65
$Fe^{2+}(aq)$	-27.9	-101.6	-90.0	-90.50
$Zn^{2+}(aq)$	-25.8	-110.4	-154.64	-147.23

Notes: Units of C_p° and S° are J mol^{-1} K^{-1}; units of ΔH_f° and ΔG_f° are kJ mol^{-1}. Aqueous cation properties are taken from Ref. [26].

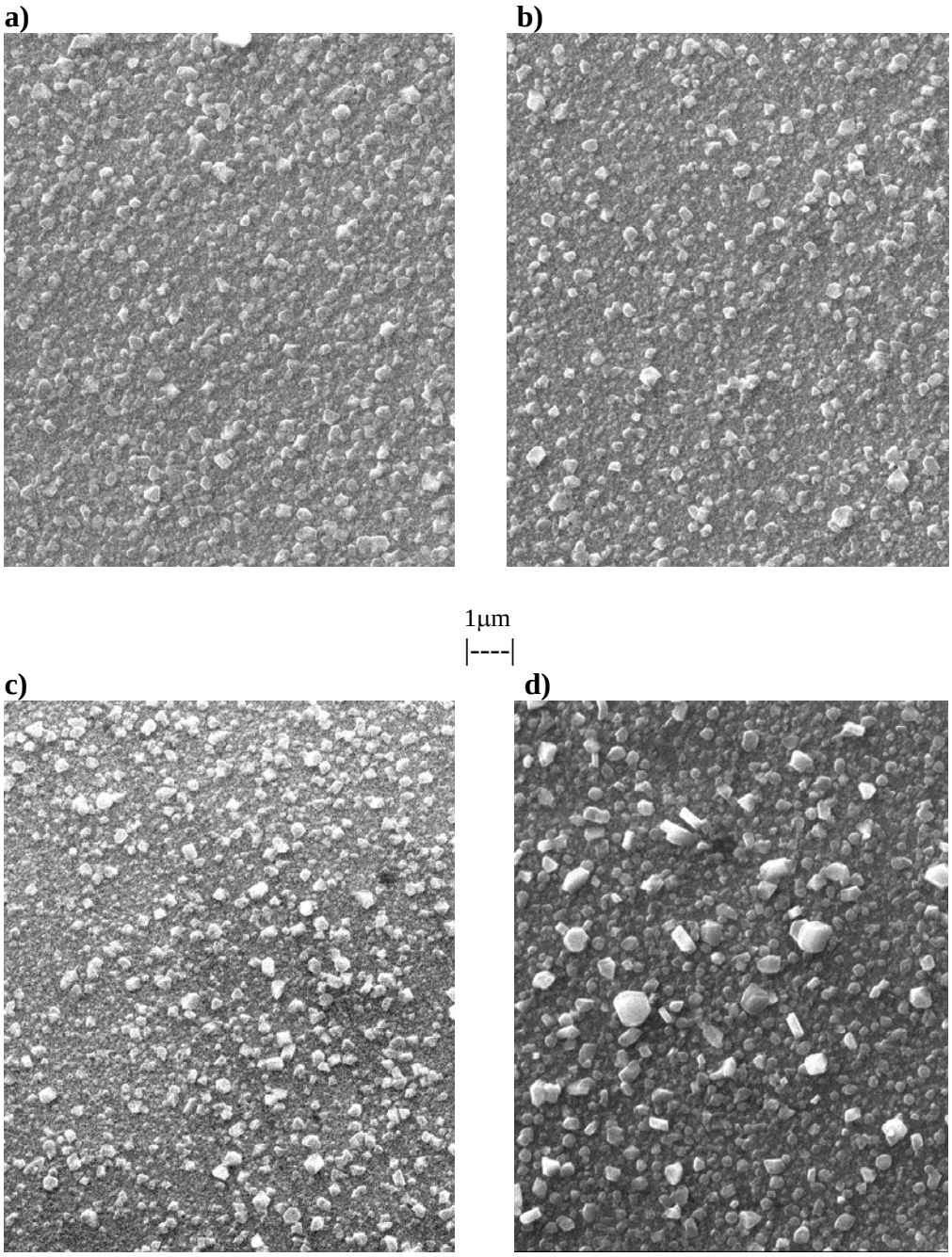

Fig. 1. High magnification SEM Photographs of 304 stainless steel after exposure to zinc treatment: (a) 1000 hr, (b) 2000 hr, (c) 5000 hr and (d) 10,000 hr.

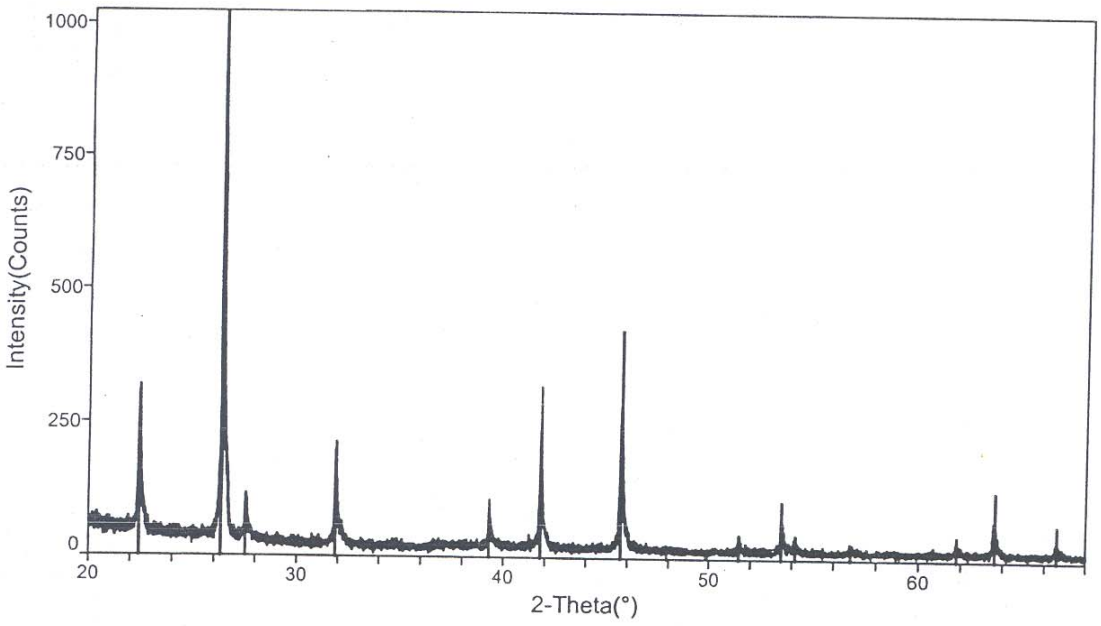

Fig. 2. Grazing incidence XRD scan (N = 0.5°) for 10,000 hr corrosion specimen (S70). All peaks can be identified as spinel phase, per comparison with PDF card 19-629 (Fe_3O_4).

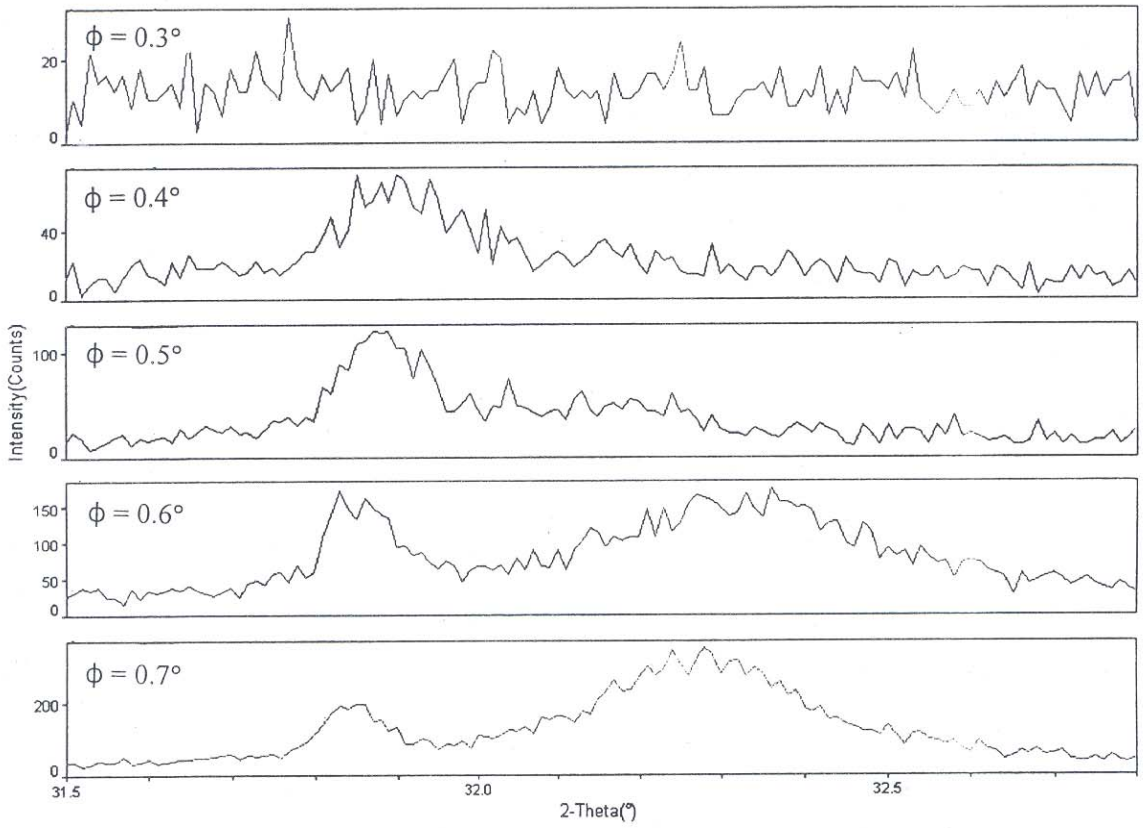

Fig. 3. Emergence of 304 stainless steel substrate [111] XRD peak in specimen S70 at incidence angles between 0.3 and 0.7°. Note appearance of substrate (2**2** = 32.3°) at N = 0.6°. The peak on the left at 2**2** = 31.85° represents the spinel [400] XRD peak.

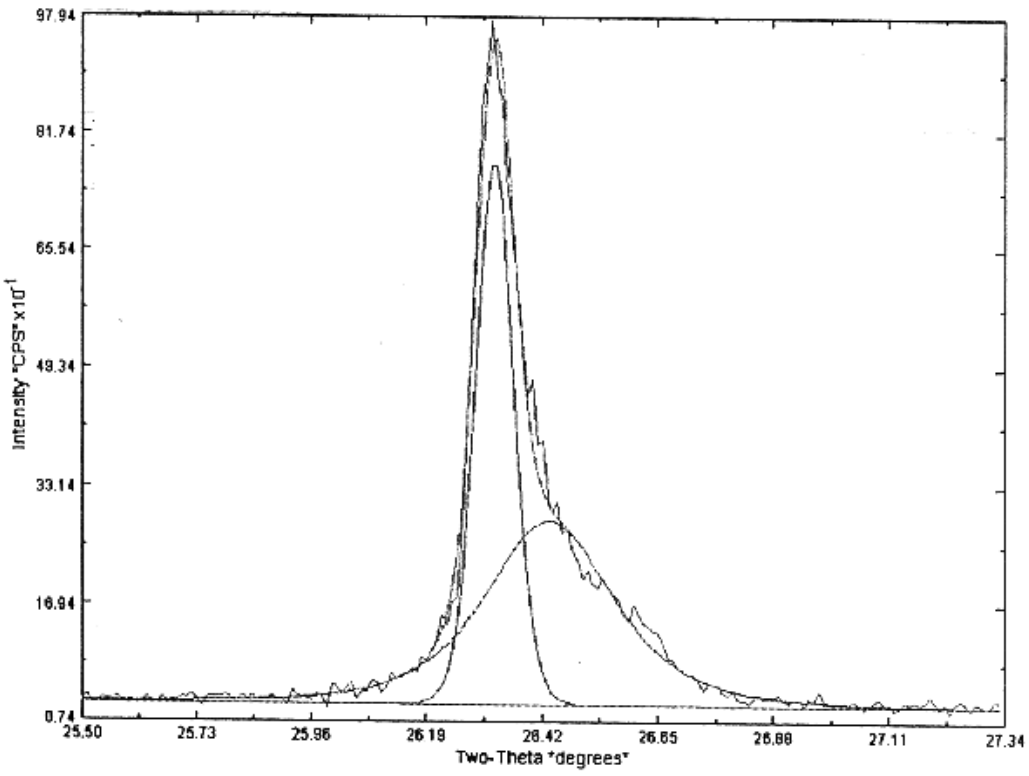

Fig. 4 High resolution plot of spinel [311] XRD peak at 2**2** = 26.2° in Fig. 2 showing asymmetric broadening on the higher 2**2** side. Each peak is believed to represent a solvus in the immiscible $(Fe_{1-n}Zn_n)Fe_2O_4$ spinel binary.

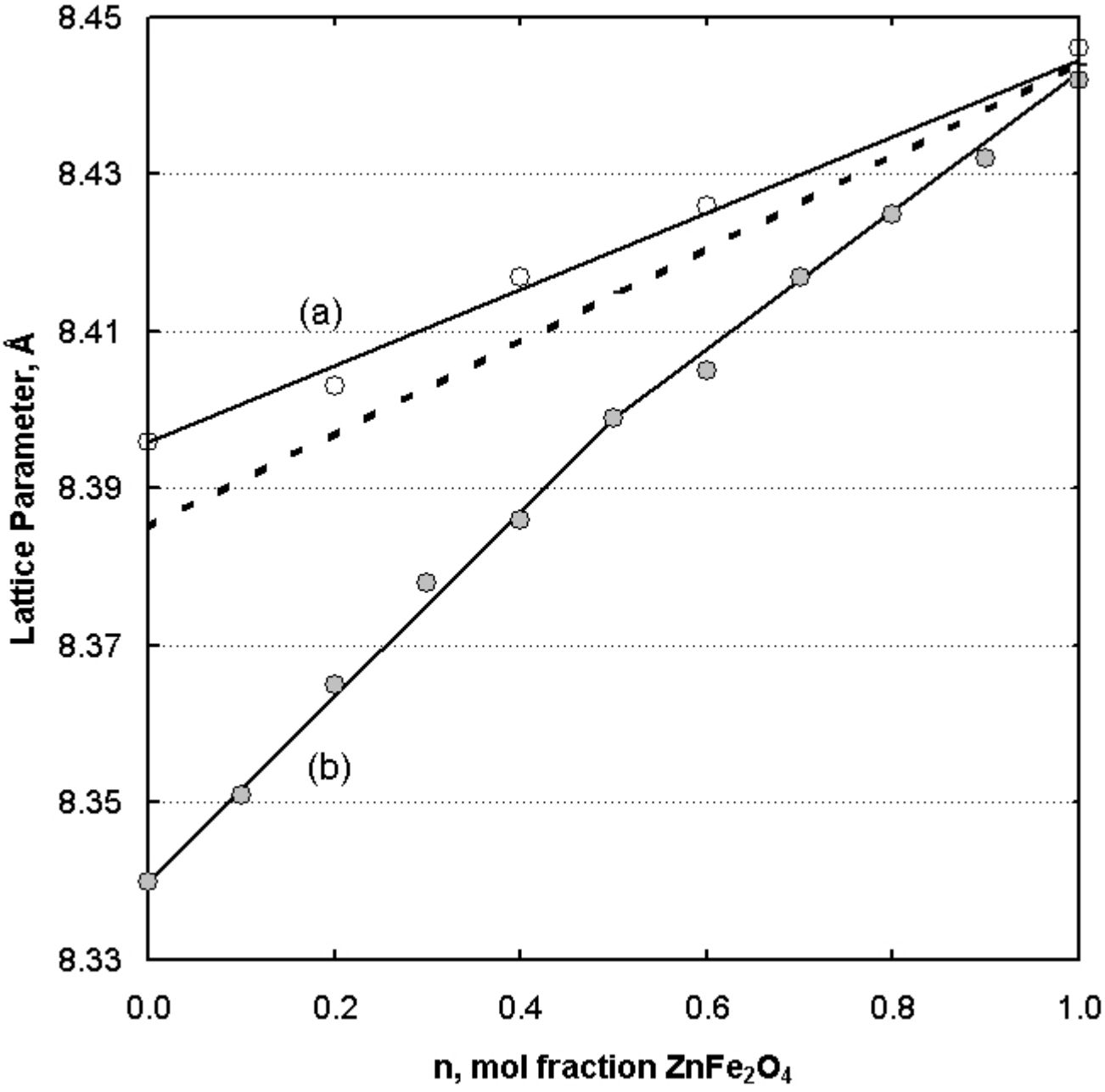

Fig. 5. Lattice parameters of ferrite binaries: (a) $(Fe_{1-n}Zn_n)Fe_2O_4$ [15] and (b) $(Ni_{1-n}Zn_n)Fe_2O_4$ [16]. Dashed line is estimate for solid solutions having Fe(II)/Ni(II) = 4.

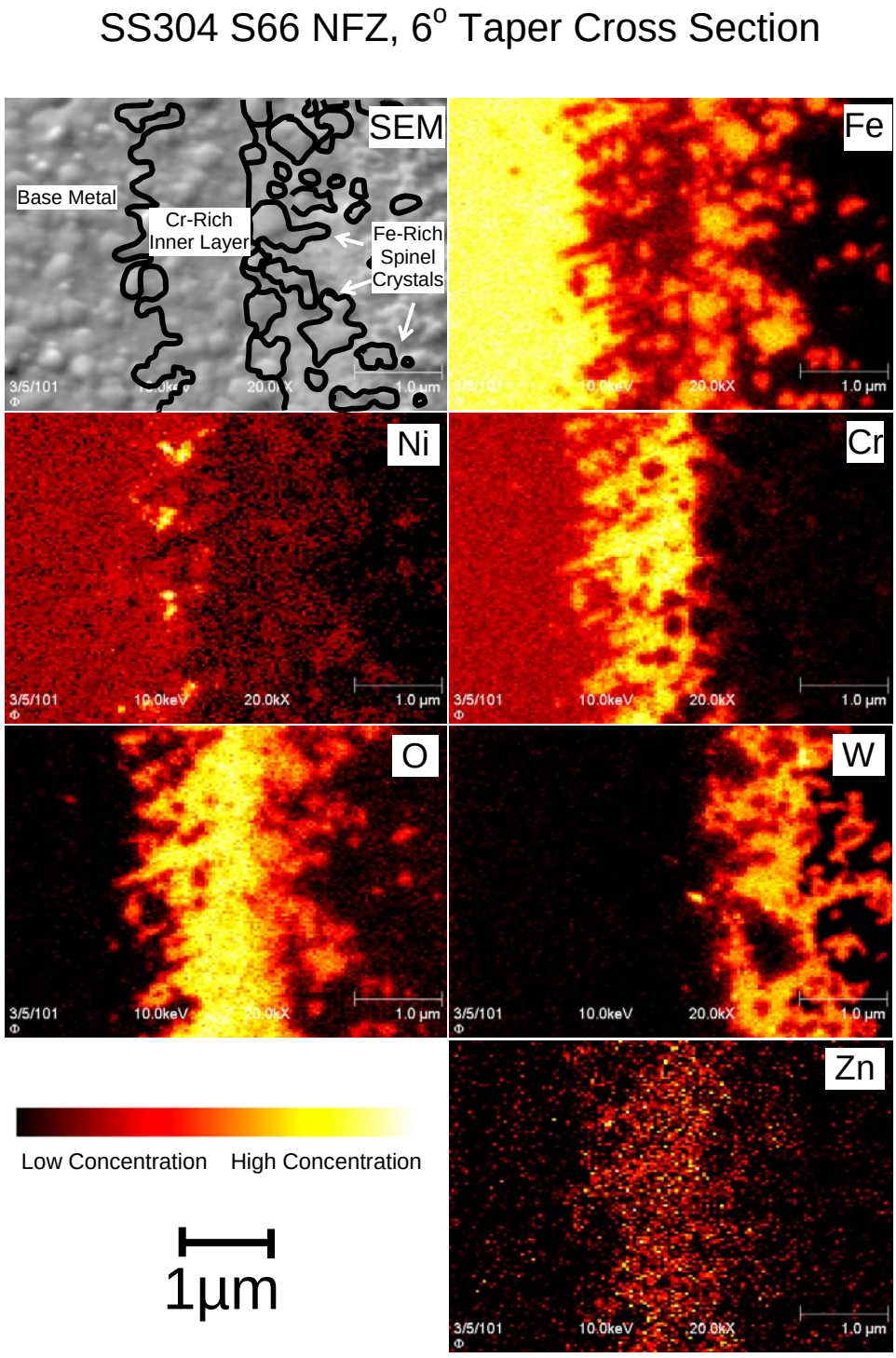

Fig. 6. Color-coded elemental Auger intensity maps of tapered cross-section of corrosion oxide on 10,000 hr specimen (S66).

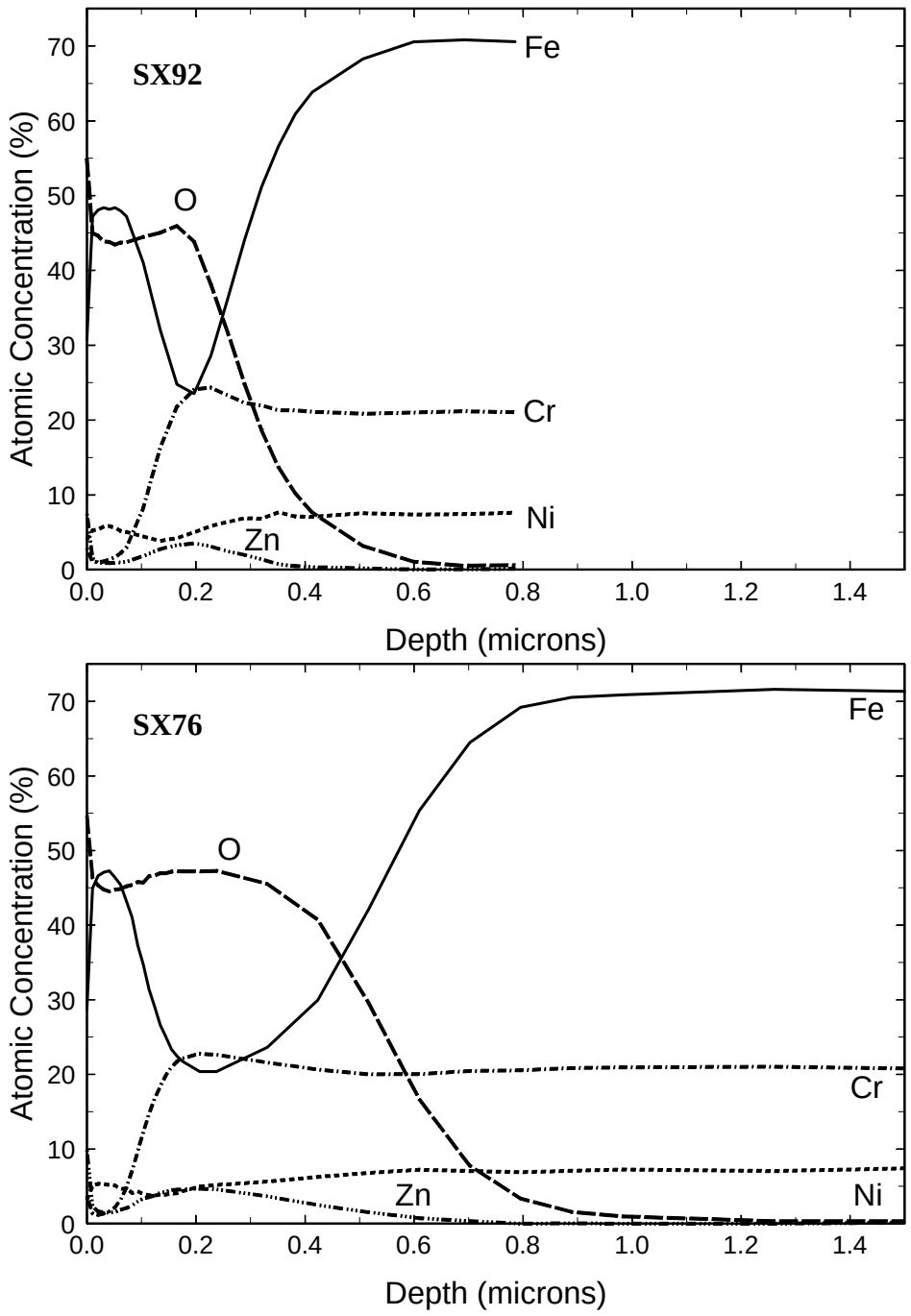

Fig. 7. Elemental composition versus depth profiles for 304 stainless steel specimens: (a) 1000 hr (SX92) and (b) 10,000 hr (SX76). Note elongated oxygen tails and wobble in the zinc profiles.

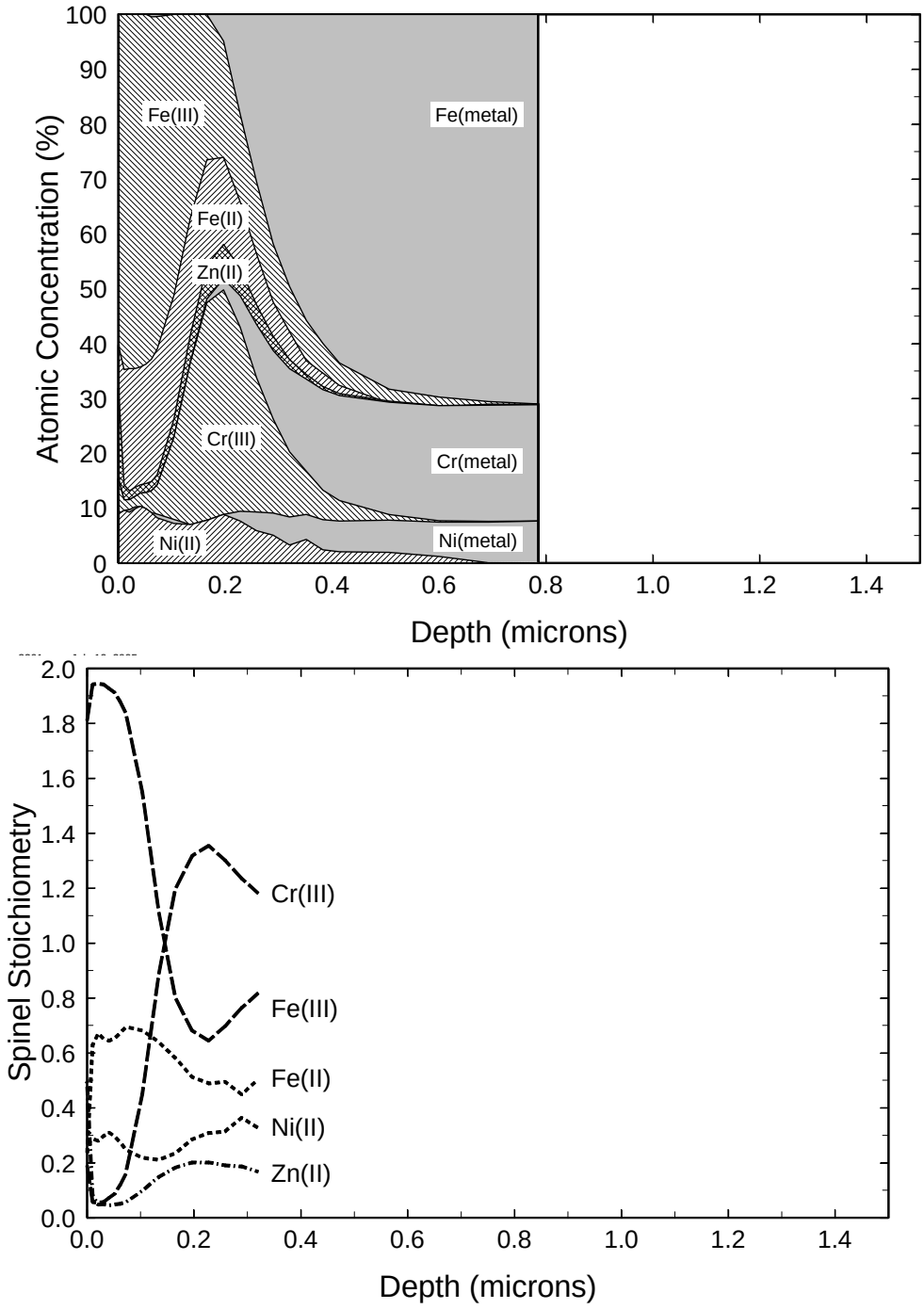

Fig. 8. Speciated composition profile of corroded 304 stainless steel surface after 1000 hr (SX92).

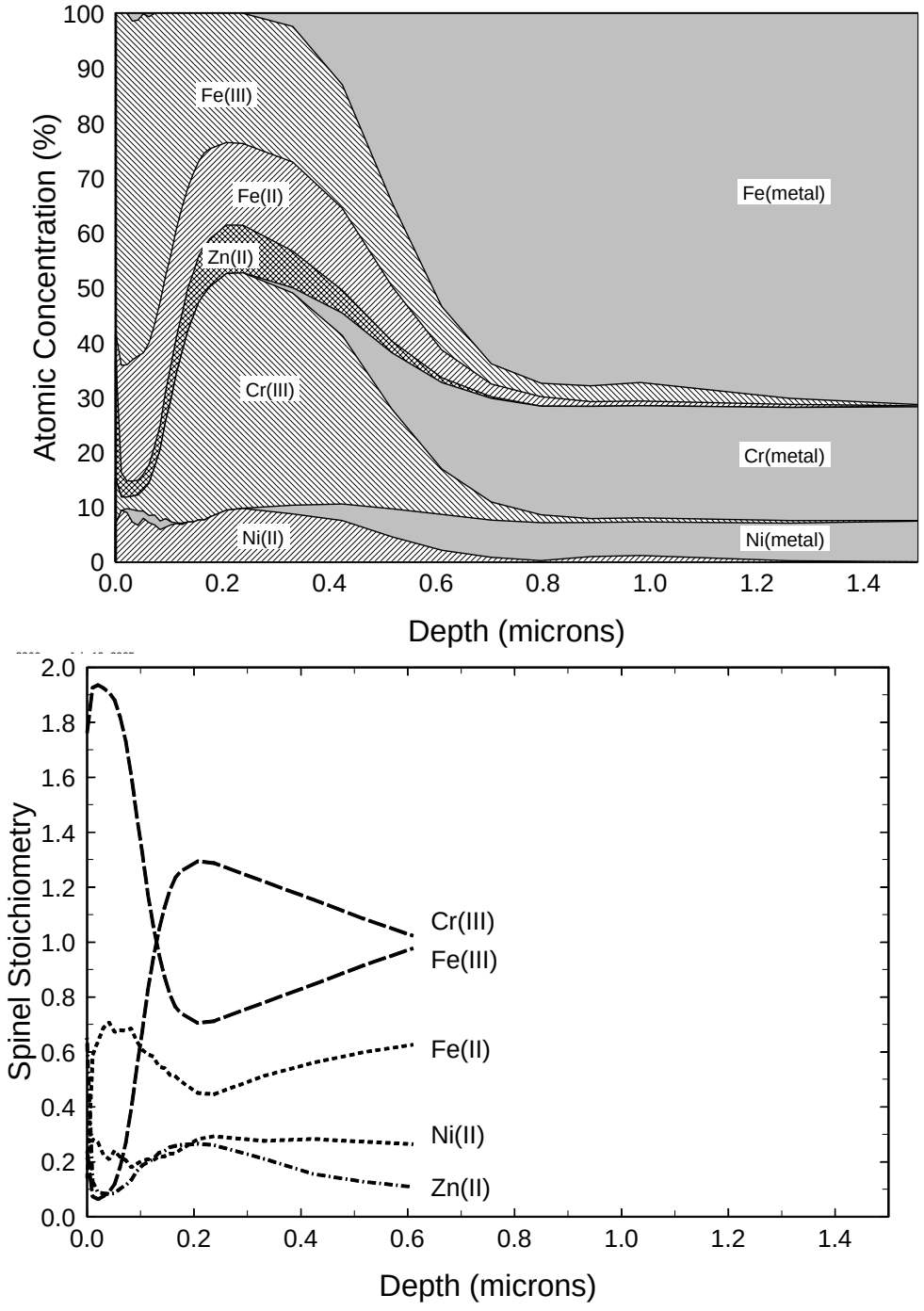

Fig. 9. Speciated composition profile of corroded 304 stainless steel surface after 10,000 hr (SX76).

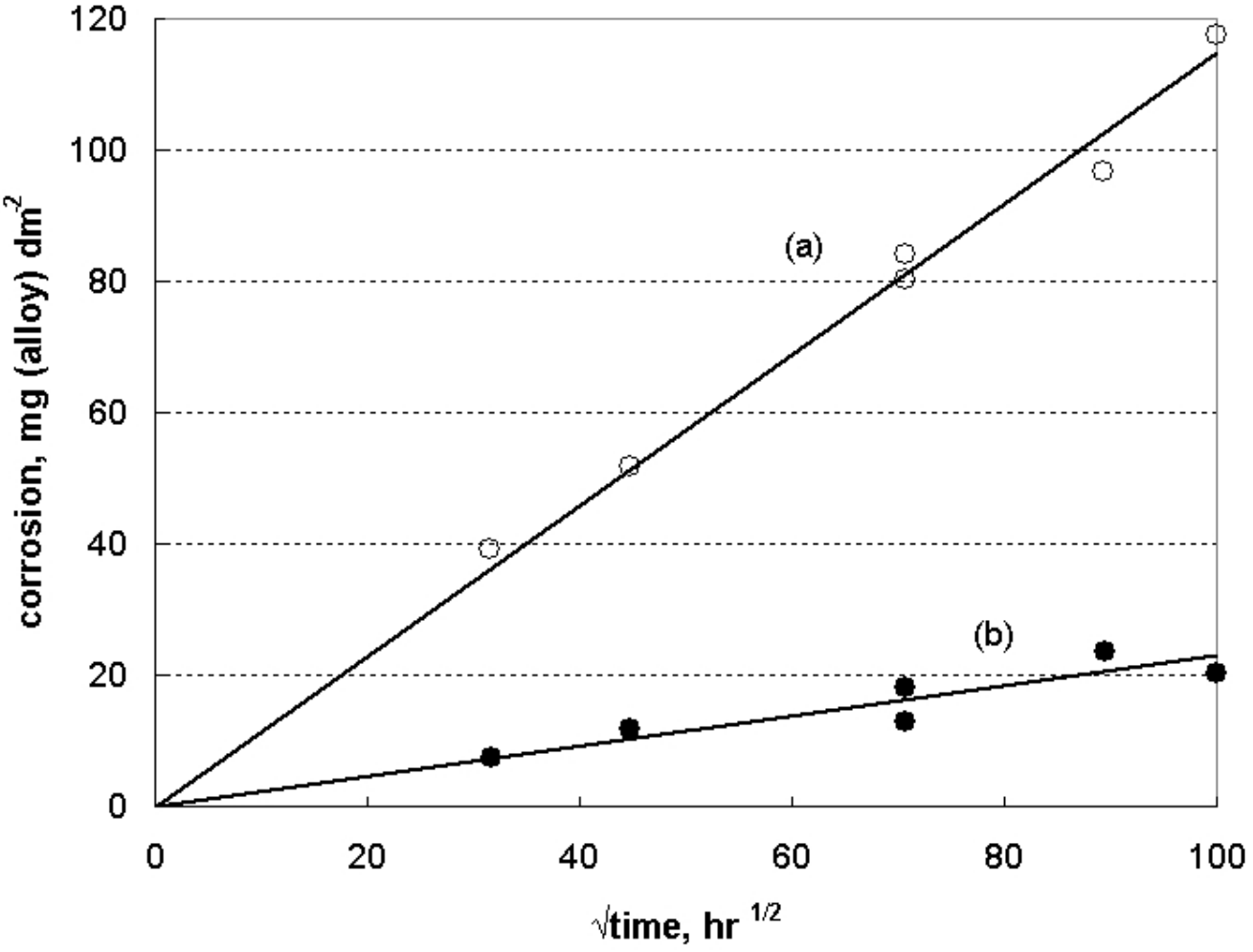

Fig. 10. Corrosion kinetics of 304 stainless steel in mildly alkaline, hydrogenated water at 260°C: (a) no zinc added [3] and (b) 30 ppb Zn(II) added.

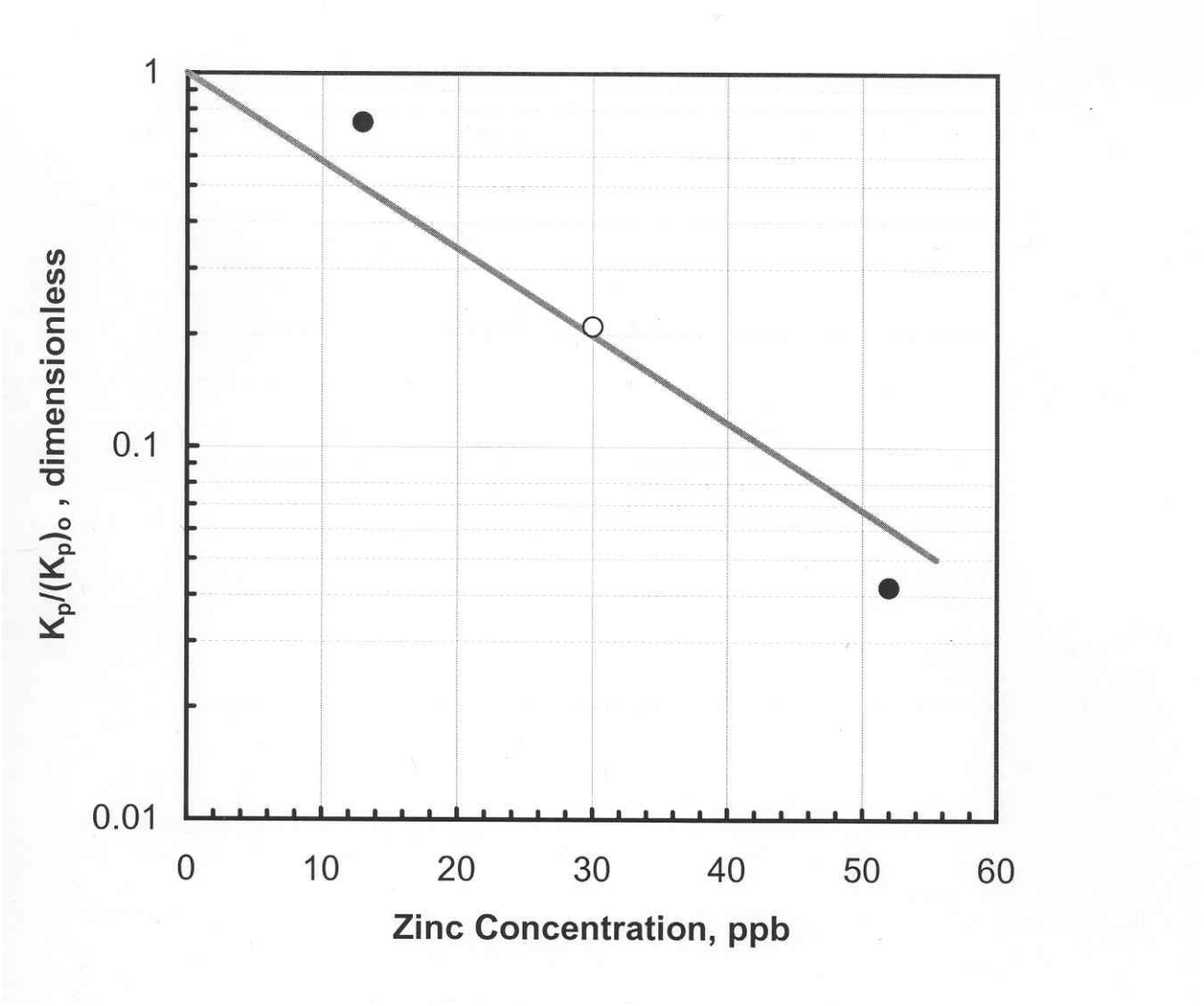

Fig. 11. Decrease in parabolic rate constant (K_p) for 304 stainless steel corrosion caused by zinc treatment: this work @ 260°C; [19] @ 288°C.

.